Intensity and polarization of dust aerosols over polarized anisotropic surfaces

K.N. Liou [a], Y. Takano [a,*], P. Yang [b]

[a] Joint Institute for Earth System Science and Engineering, Department of Atmospheric and Oceanic Sciences, University of California, Los Angeles, CA 90095, USA
[b] Department of Atmospheric Sciences, Texas A&M University, College Station, TX 77845, USA

ARTICLE INFO

ABSTRACT

The effect of surface polarization on the intensity and linear polarization patterns of sunlight in an atmosphere containing a dust aerosol layer is investigated by means of the adding principle for vector radiative transfer in which the surface is treated as a layer without transmission. We present a number of computational results and analysis for three cases: Lambertian (unpolarized isotropic), polarized isotropic, and polarized anisotropic surfaces. An approach has been developed to reconstruct anisotropic 2×2 phase matrix elements on the basis of bidirectional-reflectance and linear-polarization patterns that have been measured from polarimeters over various land surfaces. The effect of surface polarization on the simulated intensity patterns over a dust layer is shown to be negligible. However, the differences in the simulated linear polarization patterns between commonly assumed Lambertian and polarized anisotropic cases are substantial for dust optical depths between 0.1 and 0.5 and for surface albedos of 0.07 and 0.4, particularly in backward directions.

1. Introduction

Intensity and polarization of sunlight reflected from aerosols and clouds have been shown to bear a strong imprint of their size, shape, optical depth, and other optical properties. Perhaps the most intriguing results associated with the use of polarization data for inferring particle size and optical properties have been found in the study of Venus' cloud deck by the French astronomer Lyot [1]. In a subsequent work, Hansen and Hovenier [2] performed an extensive multiple scattering investigation and determined from the linear polarization data that the Venus cloud layer is composed of spherical particles (rainbow feature) having a mean radius of ~ 1.05 μm and a real refractive index of ~ 1.44 at a wavelength of 0.55 μm.

The NASA Glory mission (Mishchenko et al. [3]) had the similar idea of using the reflected spectral polarization of sunlight from the Earth's atmosphere without clouds to determine the optical and thermodynamic properties of aerosols, including absorbing black carbon and dust particles.

The NASA Glory spacecraft unfortunately failed to reach orbit after liftoff on March 4, 2011. An attempt, however, has been initiated to reengage the polarization instrument, referred to as Aerosol Polarimetric Sensor (APS), to collect polarimetric measurements along satellite ground track. In order to determine the physical and chemical properties as well as the spatial and temporal distributions of aerosols, APS will measure polarized reflected sunlight in the wavelength range of 0.4–2.4 μm. Because aerosol optical depths are usually small ($\tau < \sim 1$), it appears that the effect of surface reflection cannot be neglected, especially over bright land surfaces. Furthermore, the effect of surface polarization properties with reference to the nature of

* Corresponding author. Tel.: +1 310 794 9832; fax: +1 310 794 9796.
 E-mail address: ytakano@atmos.ucla.edu (Y. Takano).

anisotropy on polarization signals at the top of the atmosphere has not been carefully considered in radiative transfer simulations involving aerosols and thin cirrus clouds, although a number of recent studies have addressed the effect of surface polarization [4–6].

The objective of this paper is to explore the surface polarization effect on the simulated polarization patterns in an atmosphere containing dust particles. Specifically, we have extended the surface polarization model by taking into consideration recent observations of the polarized bidirectional reflectance from land surfaces. Moreover, the database for the single-scattering of dust aerosols developed by Meng et al. [7] has been used, along with the adding method for radiative transfer of polarized light to compute the reflected intensity and polarization patterns at the top of a dust layer to understand the significance of surface polarization.

This paper is organized as follows. First, we present the single-scattering properties of randomly oriented dust particles using a tri-axial ellipsoidal model in Section 2. This is followed by a discussion in Section 3 on the Stokes parameters and phase matrix in the content of vector radiative transfer using the adding/doubling approach and the definition of surface reflection matrix and its elements under various approximations. We have also presented a number of computational results and analysis for cases involving Lambertian (unpolarized isotropic), polarized isotropic, and polarized anisotropic surfaces. For the last case, an approach has been developed to reconstruct 2×2 phase matrix elements on the basis of the bidirectional-reflectance and linear-polarization patterns that have been measured over various land surfaces.

2. Optical properties of dust aerosols

Airborne mineral dust originates primarily in desert and semi-arid regions and is globally distributed. Accurate determination of its single-scattering properties is fundamental to quantifying aerosol radiative forcing and critical to developing appropriate remote sensing techniques for the detection of its size, shape, and composition. Electron microscopic images reveal that mineral dust particles are almost exclusively nonspherical and have irregular shapes with no specific habits. Due to technical difficulties, experimental determinations of the extinction efficiency, single-scattering albedo and scattering phase matrices around the forward and backward scattering directions have not been solely determined from measurements. Also, measurements are usually conducted at visible wavelengths with a small number of dust samples. The applicability of experimental approaches to the study of the single-scattering properties of dust particles throughout the entire solar and thermal infrared spectra cannot be carried out in practical terms.

Bi et al. [8] investigated the single-scattering properties of a tri-axial ellipsoidal model by introducing an additional degree of morphological freedom to reduce the symmetry of spheroids. They demonstrated that the optical properties computed from the ellipsoidal model with optimally selected particle shapes and their weightings more closely matched laboratory measurements. Additionally, the results computed from the ellipsoidal model fit measurements better than the spheroidal model, particularly in the case of the phase matrix elements associated with polarization. Meng et al. [7] developed a database for the single-scattering properties and phase matrix elements for dust particles assuming tri-axial ellipsoids based on the computational results from a combination of the T-matrix method [9], the discrete dipole approximation [10], and an improved geometric optics method [11,12]. The database covers various aspect ratios and size parameters ranging from Rayleigh to geometric optics regimes.

In the following, we discuss the scattering phase matrix for dust aerosols. If no assumption is made about particle orientation, the "scattering phase matrix" for a set of nonspherical particles contains 16 elements, P_{ij} ($i, j=1$–4), and can be expressed as follows:

$$\mathbf{P} = \begin{bmatrix} P_{11} & P_{12} & P_{13} & P_{14} \\ P_{21} & P_{22} & P_{23} & P_{24} \\ P_{31} & P_{32} & P_{33} & P_{34} \\ P_{41} & P_{42} & P_{43} & P_{44} \end{bmatrix}. \tag{1}$$

However, if nonspherical particles are assumed to be randomly oriented in space and their mirror images have equal numbers such that the reciprocity principle can be applied for incoming and outgoing light beams, the scattering phase matrix can be reduced to six independent elements in the form [13,14]

$$\mathbf{P}(\Theta) = \begin{bmatrix} P_{11} & P_{12} & 0 & 0 \\ P_{12} & P_{22} & 0 & 0 \\ 0 & 0 & P_{33} & -P_{43} \\ 0 & 0 & P_{43} & P_{44} \end{bmatrix}. \tag{2}$$

In this case, the six elements are a function of the scattering angle Θ, defined by the directions of the incoming and outgoing light beams.

In order to use the database presented in [7] for dust particles assumed ellipsoid in shape, we must specify three semi-axis lengths (a, b, and c) to define the shape, where a and b are two semi-minor and semi-major axes of the equatorial ellipse, and c is the polar radius. For a given complex refractive index m for dust, its single-scattering properties are interpolated from the database for computational purposes. Also, the database includes the kernel look-up tables $K_{sca/ext/abs}$ and K_{ij} for dust size distributions, where the notations sca, ext, and abs denote the scattering, extinction, and absorption, respectively, and ij denotes scattering phase matrix elements. For a given size distribution $dN_x/d\ln x$, the averaged scattering properties are given by

$$\bar{c}_{sca}\overline{P}_{ij}(\Theta) = \sum_m \frac{dN_x(x^m)}{d\ln x} K_{ij}(\Theta, x^m), \tag{3a}$$

$$\bar{c}_{sca/ext/abs} = \sum_m \frac{dN_x(x^m)}{d\ln x} K_{sca/ext/abs}, \tag{3b}$$

where x^m is the center of the mth bin and the size parameter x is defined by $2\pi c/\lambda$, where λ is the wavelength of incident light.

3. The adding method for vector radiative transfer including surface polarization

3.1. Background

For the transfer of a light beam including polarization contribution, we must consider the full Stokes parameters or Stokes vector [15]. A set of equations governing the diffuse reflection and transmission matrices $\mathbf{R}(\mu, \mu_0, \phi-\phi_0)$ and $\mathbf{T}(\mu, \mu_0, \phi-\phi_0)$ for the adding of two homogeneous layers with vertical optical depths τ_a and τ_b have been presented in prior literature [16–18]. The combined reflection and transmission matrices can be expressed as follows:

$$\mathbf{R}_{ab} = \mathbf{R}_a + \ \exp(-\tau_a/\mu)\mathbf{U} + \mathbf{T}_a^*\mathbf{U}, \tag{4a}$$

$$\mathbf{T}_{ab} = \exp(-\tau_b/\mu)\mathbf{D} + \mathbf{T}_b \exp(-\tau_a/\mu_0) + \mathbf{T}_b\mathbf{D}, \tag{4b}$$

where $\mathbf{D}$ and $\mathbf{U}$ correspond to the downward and upward Stokes parameters (I, Q, U, V) at an interface between the two layers, μ and μ_0 are the zenith angles for outgoing and incoming light beams, $\mathbf{T}_b$ is the transmission matrix for layer b, and $\mathbf{T}_a^*$ denotes the transmission matrix for layer a when the light beam comes from below. $\mathbf{R}_{ab}^*$ and $\mathbf{T}_{ab}^*$ can be computed from a scheme analogous to Eqs. (4a) and (4b). In adding equations, the product of two functions implies integration over an appropriate solid angle so that all possible multiple-scattering contributions can be accounted for. Moreover, for efficient computations, it is advantageous to expand the phase matrix and Stokes parameters in the Fourier series in terms of the azimuthal angle $\phi-\phi_0$. From $\mathbf{R}_{ab}$ results, we can determine the reflected intensity and polarization at the top of a scattering layer. To speed up the computations, we may set $\tau_a = \tau_b$, referred to as the doubling method. Doubling of two layers is repeated to build up a desired optical thickness starting from a thin initial layer, say on the order of 10^{-8}. $\mathbf{R}$ and $\mathbf{T}$ for a thin layer can be approximated by using the single-scattering approximation involving the "phase matrix" given by

$$\mathbf{Z}(\mu,\mu_0,\phi-\phi_0) = \mathbf{L}(\pi-i_2)\mathbf{P}(\Theta)\mathbf{L}(-i_1), \tag{5}$$

where $\mathbf{P}(\Theta)$ is the "scattering phase matrix" defined in Eq. (2), Θ is the scattering angle, and i_1 and i_2 denote the angles between meridian planes for the incoming and outgoing light beams, respectively, and the plane of scattering. The transformation matrix for the Stokes vector is given by

$$\mathbf{L}(\chi) = \begin{bmatrix} 1 & 0 & 0 & 0 \\ 0 & \cos 2\chi & \sin 2\chi & 0 \\ 0 & -\sin 2\chi & \cos 2\chi & 0 \\ 0 & 0 & 0 & 1 \end{bmatrix}, \tag{6}$$

where χ is either $\pi-i_2$ or $-i_1$. These two angles allow the transformation of the direction of the incident light beam to that of the scattered light beam. In general then, the phase matrix $\mathbf{Z}$ defined in Eq. (5) contains 16 elements. With the preceding introduction, we should now define and discuss various types of surface reflection matrices.

3.2. Surface reflection matrix

In the context of the adding principle for radiative transfer, surface can be considered as a single layer defined by a reflection matrix but without transmission so that $\mathbf{R}=\mathbf{A}$, the surface albedo matrix, and $\mathbf{T}=0$. The 16 elements of the general scattering phase matrix $\mathbf{P}$ defined in Eq. (1) for a surface without any assumption can be written in the form [13,14]

$$P_{11} = \frac{1}{2}[(M_2 + M_4) + (M_3 + M_1)],$$

$$P_{12} = \frac{1}{2}[(M_2 + M_4)-(M_3 + M_1)],$$

$$P_{13} = S_{23} + S_{41}, \quad P_{14} = -D_{23}-D_{41},$$

$$P_{21} = \frac{1}{2}[(M_2-M_4)-(M_1-M_3)],$$

$$P_{22} = \frac{1}{2}[(M_2-M_4) + (M_1-M_3)],$$

$$P_{23} = S_{23}- S_{41}, \quad P_{24} = -D_{23} + D_{41},$$

$$P_{31} = S_{24} + S_{31}, \quad P_{32} = S_{24}-S_{31},$$

$$P_{33} = S_{21} + S_{34}, \quad P_{34} = -D_{21} + D_{34},$$

$$P_{41} = D_{24} + D_{31}, \quad P_{42} = D_{24}-D_{31},$$

$$P_{43} = D_{21} + D_{34}, \quad P_{44} = S_{21}-S_{34}, \tag{7}$$

where the terms on the right-hand side of Eq. (7) are defined by

$$M_k = |S_k|^2, \quad k = 1-4,$$

$$S_{kj} = S_{jk} = \frac{1}{2}(S_j S_k^* + S_k S_j^*) = Re(S_k S_j^*), \quad j,k = 1-4, \tag{8}$$

$$-D_{kj} = D_{jk} = \frac{i}{2}(S_j S_k^*-S_k S_j^*) = Im(S_k S_j^*), \quad j,k = 1-4,$$

where * denotes the complex conjugate value. The terms S_j ($j = 1, 2, 3, 4$) are the amplitude functions which transform the incident electric field (E_{l0}, E_{r0}) to the scattered electric field (E_l, E_r) defined by

$$\begin{bmatrix} E_l \\ E_r \end{bmatrix} \propto \begin{bmatrix} S_2 & S_3 \\ S_4 & S_1 \end{bmatrix} \begin{bmatrix} E_{l0} \\ E_{r0} \end{bmatrix}. \tag{9}$$

We have presented detailed definitions of the scattering phase matrix elements which are required for analysis below.

If the normal direction of a point on the surface with respect to the tangent plane of that point defined by an angle, say ξ, is randomly distributed, and the incident and reflected light beams can be reversed [19], we may express the phase matrix similar to Eq. (2) such that it contains six independent elements, i.e. $P_{21} = P_{12} = (M_2-M_1)/2$ and $P_{43} = -P_{34} = D_{21}$.

Consider an ocean surface in which only specular reflection occurs. We should have $E_l = S_2 E_{l0}$ and $E_r = S_1 E_{r0}$ so that $S_3 = S_4 = 0$. The following phase matrix elements are defined by

$$P_{11} = P_{22} = (M_2 + M_1)/2, \ P_{33} = P_{44} = S_{21}, \ P_{43} = -P_{34} = D_{21}. \tag{10}$$

Thus, the scattering phase matrix can be expressed as

$$\mathbf{P} = \begin{bmatrix} P_{11} & P_{12} & 0 & 0 \\ P_{12} & P_{11} & 0 & 0 \\ 0 & 0 & P_{33} & -P_{43} \\ 0 & 0 & P_{43} & P_{33} \end{bmatrix}. \tag{11}$$

It follows that there are four independent phase matrix elements in this case. Furthermore, if absorption does not occur, the term $D_{21} = 0$ (see the last line in Eq. (8)), i.e. $P_{43} = 0$ so that only three independent elements remain, which is the same as those presented by Kattawar and Adams [20]. Similar to Eq. (5), the scattering phase matrices associated with the preceding conditions must be transformed from a frame of reference fixed to an ocean surface to one fixed to space in the form

$$\mathbf{A} = \mathbf{L}(\pi - \eta_r)\mathbf{PL}(-\eta_i), \tag{12}$$

where the angles η_i and η_r correspond to i_1 and i_2 as defined in Eq. (6). Thus, the matrix $\mathbf{A}$ is equivalent to the matrix $\mathbf{Z}$ defined in Eq. (5).

For a surface which reflects the incoming irradiance according to Lambert's law, its reflection matrix is given by

$$\mathbf{A} = \alpha_s \begin{bmatrix} 1 & 0 & 0 & 0 \\ 0 & 0 & 0 & 0 \\ 0 & 0 & 0 & 0 \\ 0 & 0 & 0 & 0 \end{bmatrix}, \tag{13}$$

where α_s (0–1) is the surface albedo, conventionally defined as the normalized upward flux (W/m^2). This is the case for the Lambertian ("unpolarized isotropic") surface.

In terms of the amplitude coefficients, we can set $S_1 = R_r$, $S_2 = R_l$, where R_l and R_r are the Fresnel reflection coefficients given by Eq. (5.3.23a) in Liou [14]. The matrix elements in Eq. (11) can then be expressed in the form

$$M_1 = |R_r|^2, \tag{14a}$$

$$M_2 = |R_l|^2, \tag{14b}$$

$$S_{21} = (R_l R_r^* + R_r R_l^*)/2 = Re(R_l R_r^*), \tag{14c}$$

$$D_{21} = i(R_l R_r^* - R_r R_l^*)/2 = -Im(R_l R_r^*). \tag{14d}$$

As an example, in order to see the surface polarization effect, we may set $R_l = \sqrt{0.9}$ and $R_r = -\sqrt{1.1}$. It follows that $M_1 = 1.1$ and $M_2 = 0.9$ such that $(M_1 + M_2)/2 = 1$, $(M_2 - M_1)/2 = -0.1$, $S_{21} = -\sqrt{0.9 \times 1.1} \cong -0.995$, and $D_{21} = 0$. In this manner, we have $-P_{12}/P_{11} = 0.1$. The reflection matrix can subsequently be expressed in the form

$$\mathbf{A} = \alpha_s \begin{bmatrix} 1 & -0.1 & 0 & 0 \\ -0.1 & 1 & 0 & 0 \\ 0 & 0 & -0.995 & 0 \\ 0 & 0 & 0 & -0.995 \end{bmatrix}. \tag{15}$$

In comparison with Eq. (13), the conventional definition of unpolarized isotropic surface albedo, five additional elements are included in the phase matrix. We refer to this case as "polarized isotropic surface". In the following we present a number of computational results and analysis.

In Fig. 1 we first show the scattering phase matrix elements, which were determined by interpolation from the database presented in [7]. We selected an ellipsoid shape of $a/c = 0.5$, $b/c = 0.75$, $x = 2\pi c/\lambda = 4.0$ and $m = 1.4 - i0.001$ for dust aerosols. Additionally, we have also employed an equal-volume elongated ellipsoid of $a/c = 0.35$, $b/c = 0.4$ and $x = 2\pi c/\lambda = 5.56$ for comparison. If we consider the APS 1.61-μm channel, c is ~1 and 1.4 μm for the two shapes. For the APS 0.672-μm channel, $c = $ ~0.4 and 0.6 μm. These values appear to be comparable to a typical size of dust aerosols (Ref. [21,22]), which shows the peak of the dust size distribution at ~0.5 μm. Also, the real part of the refractive index 1.4 is comparable to the value of 1.398 for mineral dust at the 1.61-μm wavelength based on interpolation of the values listed in Table 4.3 of Ref. [,22]. For the calculations involving 0.672 μm, we have used a refractive index of $1.53 - i4.28 \times 10^{-3}$. In terms of shape, we have used $a/c = 0.5$ and 0.35, and $b/c = 0.75$ and 0.4, resulting in an approximate aspect ratio of ~1.67 and 2.68. The former value is comparable to a typical aspect ratio of ~1.5 for mineral dust aerosols compiled in Ref. [23]. The phase function varies mildly as a function of the scattering angle at backscattering directions at which weakly polarizing effect of dust is shown. The degree of linear polarization (DLP), which is equivalent to $-P_{12}/P_{11}$, has positive values over all scattering angles. The term P_{22}/P_{11} is close to 1, while P_{33}/P_{11} is close to P_{44}/P_{11}. These elements vary from 1 to −1 in the scattering angle domain. The term P_{43}/P_{11} has positive and negative values at small and large scattering angles, respectively.

Fig. 2 depicts bidirectional reflectance (BR) and DLP $-Q/I$ for dust aerosols over an unpolarized isotropic (Lambertian) surface and the artificially modified surface matrix according to Eq. (15), which is polarized but isotropic. In the calculations, we used a solar incident zenith angle θ_0 of 60° and three aerosol optical depths τ_a. In the principal plane, $\phi - \phi_0 = 0°/180°$, U and V are zero. The top-left panel shows that BR values for dust aerosols over desert are larger than those over ocean for all three optical depths. At zenith angles $\theta \gtrsim -30°$, BR is close to surface albedo (0.07 or 0.4); however, for $\theta \lesssim -30°$, its values increase substantially due to grazing reflection. For the optical depth of 0.5, shown in the bottom-left panel, the effect of grazing reflection on BR at $\theta \lesssim -30°$ is enhanced by multiple scattering. In the case of isotropic ocean surface, DLP displays peaks at $\theta \approx -60°$ and 0°, as illustrated in the top-right panel. These peaks correspond to peaks of $-P_{12}/P_{11}$ at scattering angles Θ of 60° and 120° denoted in Fig. 1. In the bottom-right panel, positive polarization at forward directions ($\theta \lesssim 0°$, relative to the incident light beam) is strengthened, whereas negative polarization occurs at backward directions ($\theta \gtrsim 0°$) associated with multiple scattering. As shown in the top-right panel, positive polarization increases by ~10% due to the addition of 10% positive surface polarization in the case of optically thin dust layer ($\tau_a = 0.1$). In the bottom-right panel, positive surface polarization effect is seen to be suppressed by a thicker dust layer ($\tau_a = 0.5$), leading to reduced differences in DLP between unpolarized and polarized isotropic surfaces over both desert and ocean. Note that in order to highlight surface polarization effect, other potential effects such as
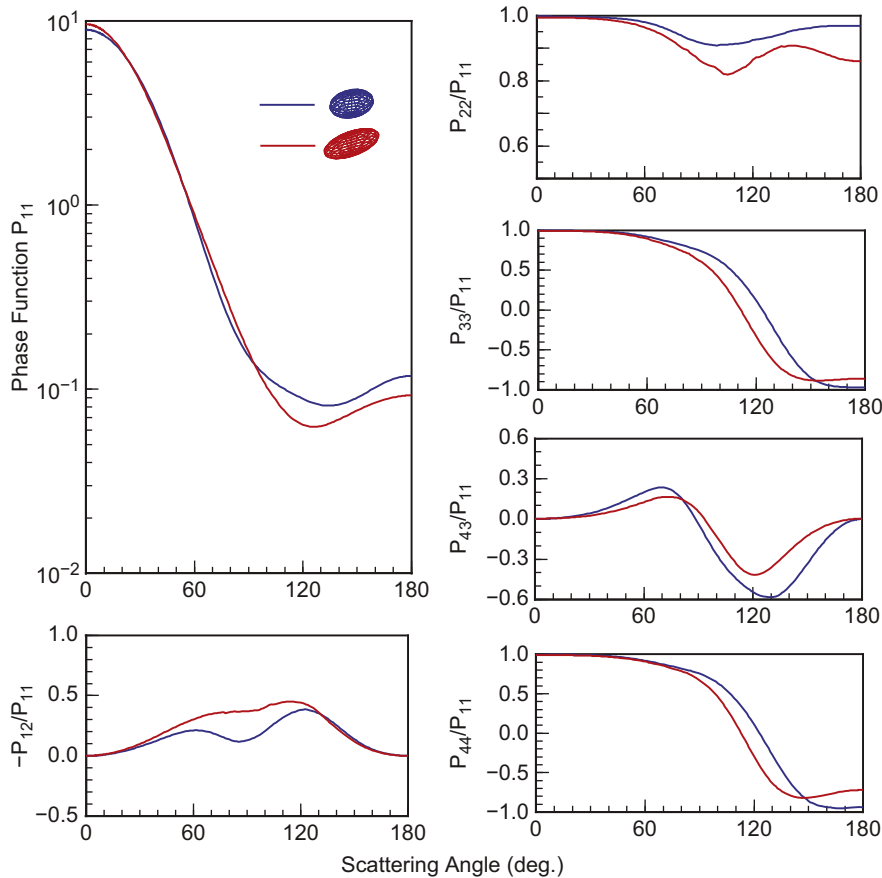
Fig. 1. Nonzero elements of the phase matrix for an ellipsoidal aerosol with $a/c=0.5$, $b/c=0.75$, $x=2\pi c/\lambda=4$ (blue line) and $a/c=0.35$, $b/c=0.4$, $x=2\pi c/\lambda=5.56$ (red line), $m=1.4-i0.001$, where a, b, and c are three semi-axes, λ is the wavelength, and m is the index of refraction. (For interpretation of references to color in this figure legend, the reader is referred to the web version of this article.)

Rayleigh scattering and water vapor absorption have not been included in the analysis and will be a subject for further study.

Now, if we neglect the P_{33} and P_{44} elements in multiple scattering computations, the 4×4 surface reflection matrix defined in Eq. (15) reduces to a 2×2 matrix in the form

$$\mathbf{A}=\alpha_s\begin{bmatrix}1 & -0.1 \\ -0.1 & 1\end{bmatrix}.\qquad(16)$$

Using this form, the results of BR and DLP differ only slightly from those presented in Fig. 2, due primarily to the fact that U and V are zero in the $\phi-\phi_0=0/180°$ plane.

In terms of surface polarization observations, only linear polarization has been measured. For example, Bréon et al. [24] measured and modeled polarized reflectance of bar soil and vegetation. However, their model was unable to reproduce negative polarization at backward directions. Wu and Zhao [25] measured polarized BR of soil and showed that all measured values are positive. More recently, Suomalainen et al. [26] and Peltoniemie et al. [27] conducted polarized BR measurements from vegetated land surfaces, soil, stones, and snow. These authors displayed observed DLP ($-Q/I$) patterns in two-dimensional space which can be used for present polarized

radiative transfer computations. Fig. 3a and b shows examples of measured $-Q/I$ of the red light reflected from a vegetated surface [26] and from sand with dead needles [27]. The results are displayed in a two-dimensional diagram in terms of two set of relevant angles with respect to the incident solar zenith angle.

In order to use these measurements in conjunction with radiative transfer in the atmosphere, we need to reconstruct phase matrix elements from linear polarization measurements to couple with the adding method for vector radiative transfer for dust layers. Consider the intensity I_s and linear polarization $-Q_s$ measured from a polarimeter. Because diffuse light was removed from I_s and Q_s [26], we should have the following matrix operation as follows:

$$\begin{bmatrix}I_s \\ Q_s\end{bmatrix}=\begin{bmatrix}A_{11} & A_{12} \\ A_{12} & A_{22}\end{bmatrix}\begin{bmatrix}I_0 \\ 0\end{bmatrix},\qquad(17)$$

where $I_0(\mu_0,\phi_0)$ is the incident solar intensity defined by the direction (μ_0,ϕ_0), so that the two phase matrix elements can be obtained from two measurements as follows:

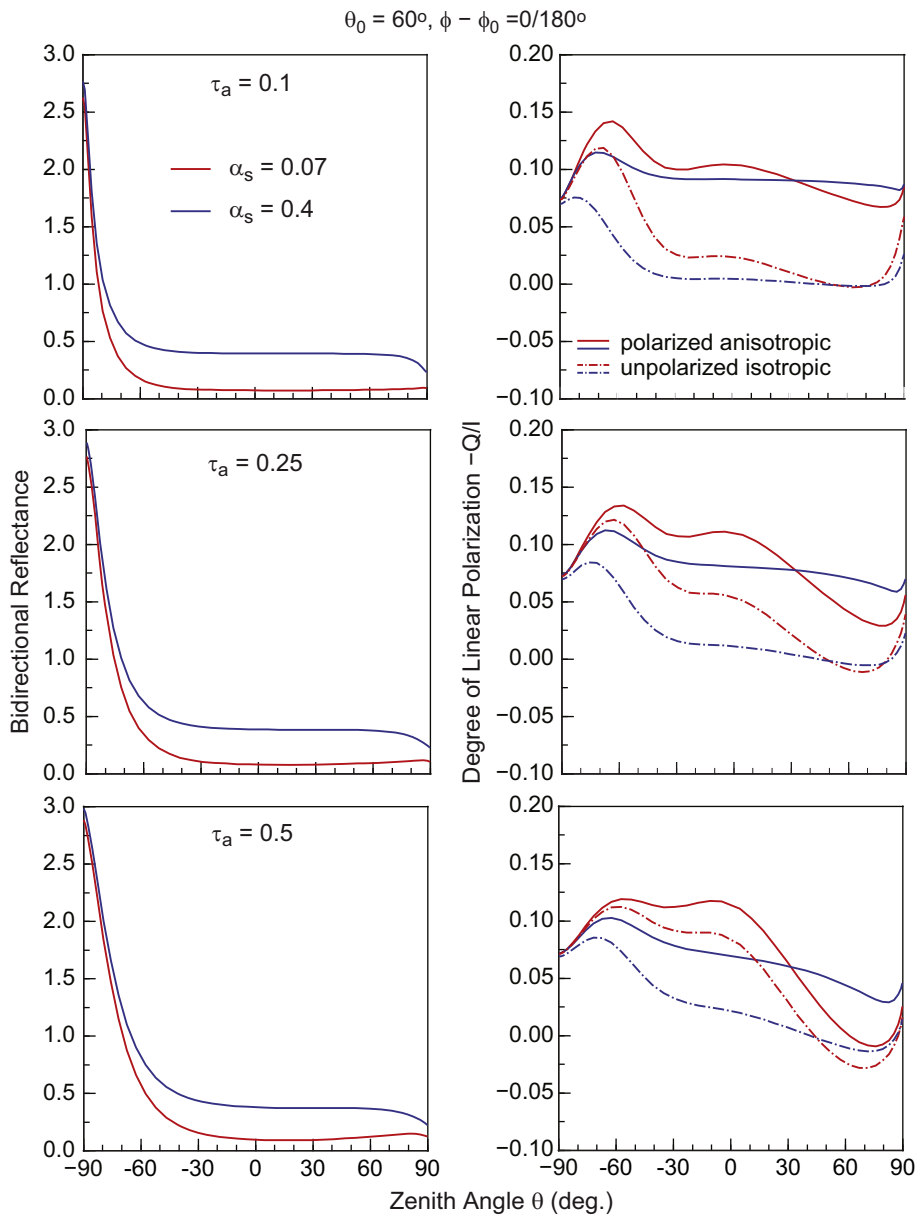$$A_{11}(\mu,\mu_0,\phi-\phi_0)=I_s(\mu,\mu_0,\phi-\phi_0)/I_0(\mu_0,\phi_0),\qquad(18a)$$

Fig. 2. Bidirectional reflectance and the degree of linear polarization $-Q/I$ as a function of zenith angle for a layer of dust aerosols overlying an unpolarized Lambertian (isotropic) surface and the polarized isotropic surface given by Eq. (15) for surface albedos of 0.07 and 0.4.

$$A_{12}(\mu, \mu_0, \phi-\phi_0) = Q_s(\mu, \mu_0, \phi-\phi_0)/I_0(\mu_0, \phi_0). \quad (18b)$$

Note that the direction of the reflected light beam is represented by the two-dimensional angular function $(\mu, \mu_0, \phi-\phi_0)$ for the two phase matrix elements. This is the case which is referred to as "polarized anisotropic." The conventional surface albedo cannot be defined in this case. Also, the third element A_{22} cannot be determined from two measurements (BR and DLP); however, to a good approximation, we may set $A_{22} \sim A_{11}$ (see the curve P_{22}/P_{11} in Fig. 1).

By definition, A_{11} is equivalent to BR and $-A_{12}$ represents DLP measurements displayed in Fig. 3 based on which we have developed an analytical equation to

parameterize A_{12} values in the form

$$A_{12} = -C\left(\frac{2\theta}{\pi}\right)\cos(\phi-\phi_0), \quad (19)$$

where C is a constant, θ is zenith angle confined to $[0, \pi/2]$, and $\phi-\phi_0$ is the azimuthal angle in the range of $[-\pi, \pi]$. From Fig. 3a and b, C is about 0.05 and 0.1. Results of the parameterization are depicted on the right-hand side of Fig. 3a and b, representing the two-dimensional domain consisting of the reflected zenith angle θ and relative azimuthal angle $\phi-\phi_0$. In the principal plane $\phi-\phi_0=0°/180°$ in the left panel of Fig. 3a, the observed $-Q_s/I_s$ is positive, with values smaller than 0.05, at $\theta < 0°$ (i.e., in the plane $\phi-\phi_0=0°$), almost zero at $\theta=0°$ (i.e., at the zenith),
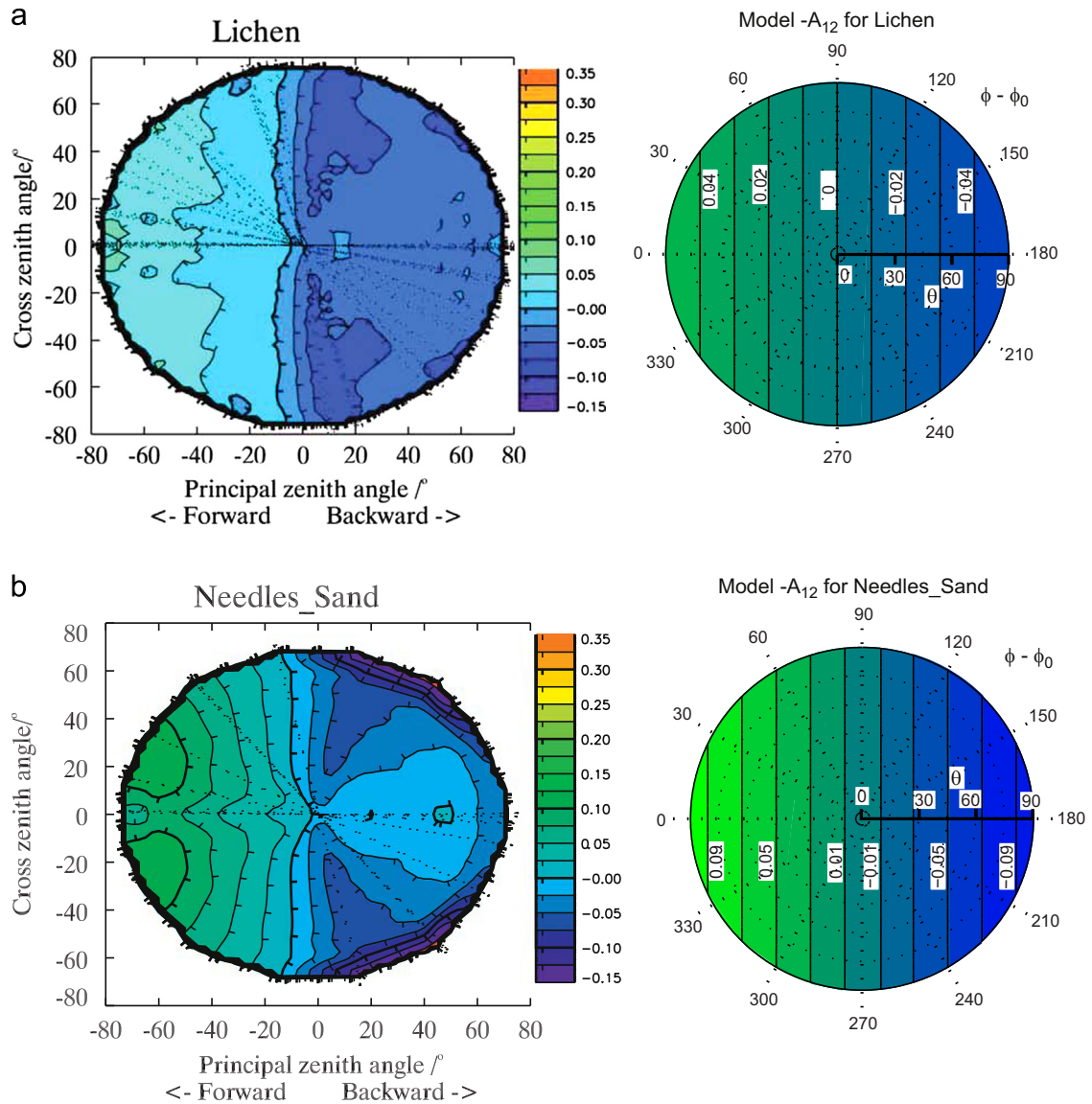
Fig. 3. Linear polarization ($-Q_s/I_s$) patterns of the red light reflected from a vegetated surface (a) measured by Suomalainen et al. [26] in which the solar zenith angle was from $45°$ to $47°$ and from a sand surface with dead needles (b) measured by Peltoniemi et al. [27] in which the incident solar zenith angle was $55°$. The right diagrams illustrate the results determined from parameterization [Eq. (19)] in the zenith and azimuthal angle domain.

and negative, also with absolute values smaller than 0.05 but with more variability, at $\theta > 0°$ (i.e., in the plane $\phi-\phi_0 = 180°$), which were shown at the top-right panel in Fig. 3 of Ref. [26]. This behavior is approximately reproduced in the right panel in Fig. 3 based on an analytical model developed in this paper with an overall accuracy of about 10% without capturing detailed features in the measured data. See also Figs. 3–10 in Ref. [26] and Figs. 8–11 in Ref. [27], which show the same behavior. The parameterized Eq. (19) is useful for the interpretation of $-Q/I$ in the principal plane $\phi-\phi_0 = 0°/180°$ presented in Fig. 4. Also, dependence of the observed $-Q_s/I_s$ on wavelength is relatively weak [26,27]. For this reason, the surface polarization ($-Q_s/I_s$) pattern at $0.67\ \mu m$ shown in Fig. 3 can be applied to near infrared wavelengths as well. We also note that the BR measurements depicted in

Suomalainen et al. [26] and Peltoniemie et al. [27] are complicated three-dimensional functions. However, their values are all close to a constant value.

Fig. 4a shows comparison of BR and DLP at the top of dust layers between unpolarized isotropic surface and the polarized anisotropic surface defined by Eq. (19) with $C = 0.1$, corresponding to the results presented in Fig. 3b. Anisotropic surface polarization does not affect BR, similar to the results shown in Fig. 2. For an optically thin dust layer ($\tau_a = 0.1$) depicted in the top-right panel, stronger positive and negative polarization patterns are shown, respectively, at forward and backward directions in comparison to the isotropic unpolarized surface case. Negative polarization at backscattering directions results from the surface polarization effect shown in Fig. 3b. For $\tau_a = 0.5$, displayed in the bottom-right panel, negative polarization
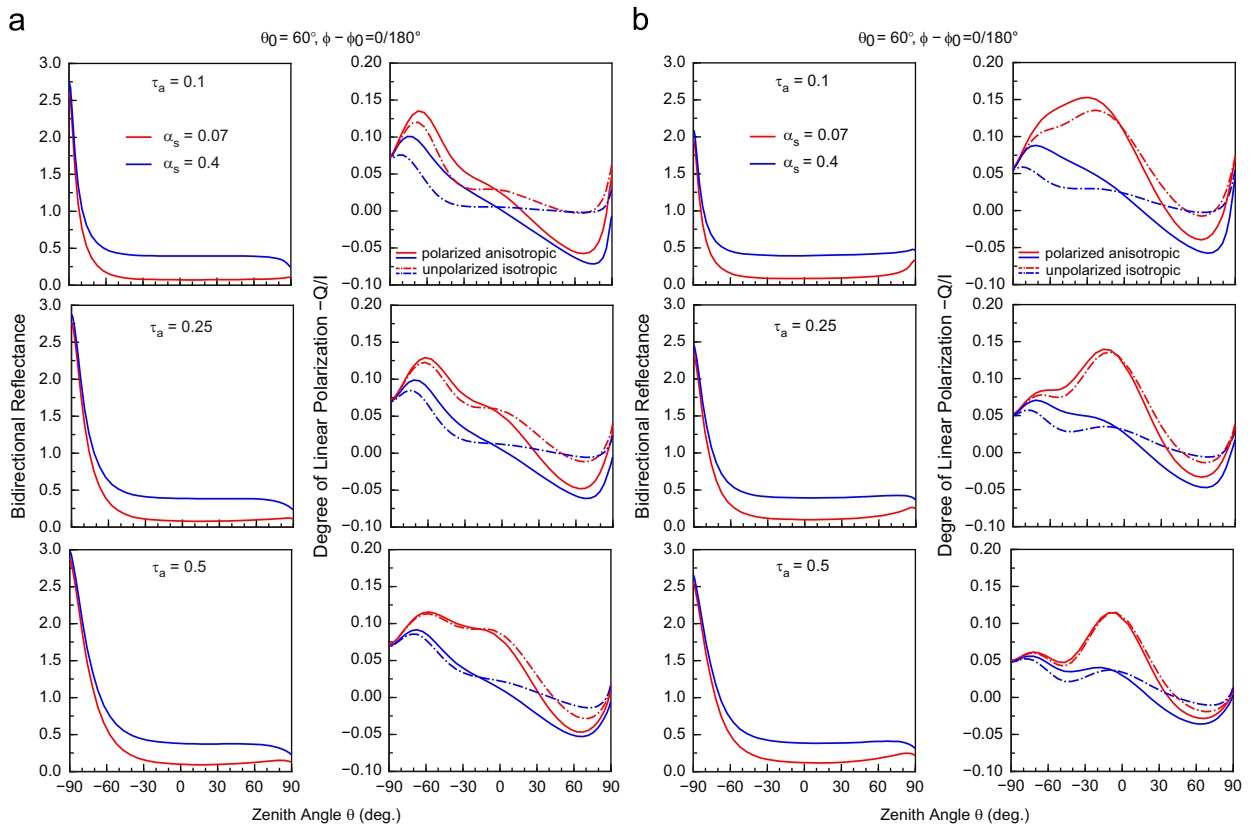
Fig. 4. (a) Bidirectional reflectance and the degree of linear polarization $-Q/I$ as a function of zenith angle for a dust layer overlying an unpolarized isotropic surface and the polarized anisotropic surface defined by Eq. (19) with $C=0.1$ for two surface albedos of 0.07 and 0.4 at 1.61 μm wavelength. Rayleigh scattering contributions are included, but are negligible in this case. (b) Bidirectional reflectance and the degree of linear polarization $-Q/I$ as a function of zenith angle for a dust layer overlying an unpolarized isotropic surface and the polarized anisotropic surface defined by Eq. (19) with $C=0.1$ for two surface albedos of 0.07 and 0.4 at 0.672 μm wavelength. Rayleigh scattering contributions are included.

at backward directions is reduced due to multiple scattering, which differs from those presented in Fig. 2. When C is set to 0.05 in Eq. (19), DLP values are between $C=0.1$ and unpolarized isotropic surface cases. Despite subtle differences in the phase function and $-P_{12}/P_{11}$ between the two ellipsoids displayed in Fig. 1, the simulated BR and DLP patterns for elongated ellipsoid are substantially similar to those presented in Fig. 4a, particularly at backward directions with reference to aerosol optical depth for an anisotropically polarized surface in comparison to an isotropic unpolarized (Lambertian) surface. For the 1.61-μm wavelength, the Rayleigh optical depth is 0.0013, which is much smaller than aerosol optical depths ≥0.1 employed in this paper. As a result, the simulated BR and DLP in Fig. 4a are essentially the same as in the case in which Rayleigh scattering is neglected. For the 0.672-μm wavelength shown in Fig. 4b, the Rayleigh optical depth is 0.043. The simulated BR patterns remain approximately the same as those depicted in Fig. 4a; however, the DLP increases substantially in the zenith angle region of −30–30° in the case of an albedo of 0.07. In the region of 30–60° (backscattering directions), the results are similar to those shown in Fig. 4a. For a higher albedo of 0.4, the results displayed in Fig. 4a and b are similar.

4. Concluding remarks

We investigate surface polarization effect on the simulation of intensity and linear polarization patterns above a dust aerosol layer using the adding principle for vector radiative transfer, which represents a first step to understand the anisotropic surface effects on polarization patterns of dusty atmospheres. In the formulation, surface is considered to be a layer defined by a reflection matrix but without transmission. Dust particles are assumed to be randomly-oriented tri-axial ellipsoids based on which the scattering phase matrix consists of six independent elements. In the analysis of surface reflection matrix, we consider three surface types: Lambertian (unpolarized isotropic, commonly assumed), polarized isotropic, and polarized anisotropic. We focus on linear polarization that has been observed over various land surfaces, and develop an approach to invert BR and DLP measured values to obtain 2×2 phase matrix elements that are required for vector radiative transfer calculations.

The surface polarization effect on the simulated intensity patterns over a dust layer is shown to be negligible. However, differences in the simulated linear polarization patterns between commonly assumed Lambertian and

polarized anisotropic cases are substantial for dust optical depths between 0.1 and 0.5 and covering surface albedo from 0.07 to 0.4, particularly in backscattering directions relative to the Sun's position. In order to make precise spectral polarization calculations to interpret measurements from space in the UV, visible, and near infrared wavelengths for the purposes of determining the size, shape, and single-scattering albedo of various types of aerosols, including black carbon, it is critically important to account for the surface polarization effect: a conclusion in line with the recent work on the polarimetric modeling of surface properties and the polarimetric retrievals of aerosol properties over land [28–30].

Acknowledgments

References

[1] Lyot B. Recherches sur la polarisation de la lumière des planètes et de quelques substances terrestres. Ann Obs Paris (Meudon) 1929;8. 161 p. [available in English as NASA TTF-187, 1964].

[2] Hansen JE, Hovenier JW. Interpretation of the polarization of Venus. J Atmos Sci 1974;31:1137–60.

[3] Mishchenko MI, Cairns B, Kopp G, Schueler CF, Fafaul BA, Hansen JE, et al. Accurate monitoring of terrestrial aerosols and total solar irradiance: introducing the Glory mission. Bull Am Meteorol Soc 2007;88:677–91.

[4] Waquet F, Goloub P, Deuzé J-L, Léon J-F, Auriol F, Verwaerde C, et al. Aerosol retrieval over land using a multiband polarimeter and comparison with path radiance method. J Geophys Res 2007;112: D11214. http://dx.doi.org/10.1029/2006JD008029.

[5] Waquet F, Cairns B, Knobelspiesse K, Chowdhary J, Travis LD, Schmid B, et al. Polarimetric remote sensing of aerosols over land. J Geophys Res 2009;114:D01206. http://dx.doi.org/10.1029/2008JD010619.

[6] Diner DJ, Xu F, Martonchik JV, Rheingans BE, Geier S, Jovanovic VM, et al. Exploration of a polarized surface bidirectional reflectance model using the ground-based multiangle spectropolarimetric imager. Atmosphere 2012;3:591–619.

[7] Meng Z, Yang P, Kattawar GW, Bi L, Liou KN, Laszlo I. Single-scattering properties of tri-axial ellipsoidal mineral dust aerosols: a database for application to radiative transfer calculations. J Aerosol Sci 2010;41:501–12.

[8] Bi L, Yang P, Kattawar GW, Kahn R. Single-scattering properties of triaxial ellipsoidal particles for a size parameter range from the Rayleigh to geometric-optics regimes. Appl Opt 2009;48:114–26.

[9] Mishchenko MI, Travis LD, Mackowski DW. *T*-matrix method and its applications to electromagnetic scattering by particles: a current perspective. J Quant Spectrosc Radiat Transfer 2010;115:1700–3.

[10] Draine BT, Flatau PJ. Discrete-dipole approximation for scattering calculations. J Opt Soc Am A 1994;11:1491–9.

[11] Yang P, Liou KN. A geometric-optics/integral-equation method for light scattering by nonspherical ice crystals. Appl Opt 1996;35: 6568–84.

[12] Yang P, Liou KN. Light scattering by hexagonal ice crystals: solutions by a ray-by-ray integration algorithm. J Opt Soc Am A 1997;14: 2278–89.

[13] van de Hulst HC. Light scattering by small particles. New York: Wiley; 1957.

[14] Liou KN. An introduction to atmospheric radiation. 2nd ed. San Diego: Academic Press; 2002.

[15] Stokes GG. On the composition and resolution of streams of polarized light from different sources. Trans Cambridge Philos Soc 1852;9:339–416.

[16] Liou KN. Applications of the discrete-ordinates method for radiative transfer to inhomogeneous aerosol atmospheres. J Geophys Res 1975;80:3434–40.

[17] Takano Y, Liou KN. Solar radiative transfer in cirrus clouds. Part II. Theory and computation of multiple scattering in an anisotropic medium. J Atmos Sci 1989;46:20–36.

[18] Liou KN, Takano Y. Interpretation of cirrus cloud polarization measurements from radiative transfer theory. Geophys Res Lett 2002;29:p. 27-1–4. http://dx.doi.org/10.1029/2001GL014613.

[19] Perrin P. Polarization of light scattered by isotropic opalescent media. J Chem Phys 1942;10:415–26.

[20] Kattawar GW, Adams CN. Stokes vector calculations of the submarine light field in an atmosphere-ocean with scattering according to a Rayleigh phase matrix: effect of interface refractive index on radiance and polarization. Limnol Oceanogr 1989;34:1453–72.

[21] Hansen JE, Travis LD. Light scattering in planetary atmosphere. Space Sci Rev 1974;16:527–610.

[22] d'Almeida GA, Koepke P, Shettle EP. Atmospheric aerosols. Hampton: Deepack; 1991.

[23] Ginoux P. Effects of nonsphericity on mineral dust modeling. J Geophys Res 2003;108:4052. http://dx.doi.org/10.1029/2002JD002516.

[24] Bréon RM, Tanre D, Lecomte P, Herman M. Polarized reflectance of bare soils and vegetation: measurements and models. IEEE Trans Geosci Remote Sensing 1995;33:487–99.

[25] Wu T, Zhao Y. The bidirectional polarized reflectance model of soil. IEEE Trans Geosci Remote Sensing 2005;43:2854–9.

[26] Suomalainen J, Hakala T, Puttonen E, Peltoniemi J. Polarised bidirectional reflectance factor measurements from vegetated land surfaces. J Quant Spectrosc Radiat Transfer 2009;110:1044–56.

[27] Peltoniemi J, Hakala T, Suomalainen J, Puttonen E. Polarised bidirectional reflectance factor measurements from soil, stones, and snow. J Quant Spectrosc Radiat Transfer 2009;110:1940–53.

[28] Litvinov P, Hasekamp O, Cairns B, Mishchenko MI. Reflection models for soil and vegetation surfaces from multiple-viewing angle photopolarimetric measurements. J Quant Spectrosc Radiat Transfer 2010;111:529–39.

[29] Litvinov P, Hasekamp O, Cairns B. Models for surface reflection of radiance and polarized radiance: comparison with airborne multi-angle photopolarimetric measurements and implications for modeling top-of-atmosphere measurements. Remote Sensing Environ 2011;115:781–92.

[30] Litvinov P, Hasekamp O, Dubovik O, Cairns B. Model for land surface reflectance treatment: physical derivation, application for bare soil and evaluation on airborne and satellite measurements. J Quant Spectrosc Radiat Transfer 2012;113:2023–39.